Enhancement of weak ferromagnetism, exotic structure prediction and diverse electronic properties in holmium substituted multiferroic bismuth ferrite

Čebela, Marija; Zagorac, Dejan; Popov, Igor; Torić, Filip; Klaser, Teodoro; Skoko, Željko; Pajić, Damir

Enhancement of weak ferromagnetism, exotic structure prediction and diverse electronic properties in holmium substituted multiferroic bismuth ferrite

Maria Čebela[1,2,3*], Dejan Zagorac[2,3*], Igor Popov[4,5*], Filip Torić[1], Teodoro Klaser[6], Željko Skoko[1], Damir Pajić[1*]

[1] University of Zagreb, Faculty of Science, Department of Physics, Bijenička cesta 32, 10000 Zagreb, Croatia

[2] Materials Science Laboratory, Institute of Nuclear Sciences Vinča, University of Belgrade, National Institute of the Republic of Serbia, Mike Petrovića Alasa 12-14, Belgrade, Serbia

[3] Center of Excellence "CextremeLab", Institute of Nuclear Sciences Vinča, University of Belgrade, National Institute of the Republic of Serbia, Mike Petrovića Alasa 12-14, Belgrade, Serbia

[4] Institute for Multidisciplinary Research, University of Belgrade, Kneza Višeslava 1, 11030 Belgrade, Serbia

[5] Institute of Physics, University of Belgrade, Pregrevica 118, 11080 Belgrade, Serbia

[6] Ruđer Bošković Institute, Bijenička cesta 54, 10000 Zagreb, Croatia

Corresponding Authors: mcebela@vinca.rs , dzagorac@vinca.rs , popov@ipb.ac.rs , dpajic@phy.hr

Abstract

Bismuth ferrite (BFO, $BiFeO_3$), exhibiting both ferromagnetic and ferroelectric properties at room temperature, is one of the most researched multiferroic materials with a growing number of technological applications. In the present study, using a combined theoretical-experimental approach, we have investigated the influence of Ho-doping on BFO structural, electronic and magnetic properties. Synthesis and structural XRD characterization of $Bi_{1-x}Ho_xFeO_3$ (x= 0.02, 0.05, 0.10) nanopowders have been completed. After structure prediction of Ho-doped $BiFeO_3$ using bond valence calculations (BVC) calculations six most favorable candidates were found: α-, β-, γ-, R-, T1, and T2. Furthermore, all structure candidates have been examined for different magnetic ordering using the DFT calculations. The magnetic behavior of the synthesized materials was investigated using a SQUID magnetometer equipped with an oven. The plethora of magnetic and electronic properties of the Ho-doped BFO that our theoretical research predicted can open rich possibilities for further investigation and eventual applications.

Keywords: Structure-property relationships, Electronic structure, Magnetic properties, Weak ferromagnetism, X-ray diffraction (XRD)

1. Introduction

Multiferroic materials are materials that occur in more than one ferroic order.[1] Among these materials, the most interesting ones are those which possess magnetic and electric order simultaneously. Materials in which magnetic and electric properties are coupled are referred to as magnetoelectrics.[1] Simultaneous control and tuning of the magnetic properties by an electric field and vice versa opens a vast scope of potential applications such as magnetic memories and spintronics. [2, 3]

Among these magnetoelectric materials, $BiFeO_3$ stands as a role model for research potential applications as it shows multiferroic properties at room temperature with the antiferromagnetic transition at 640 K and ferroelectric transition at 1100 K. $BiFeO_3$ stands also as a building model for investigating different doping approaches for enhancing its multiferroic properties.[4] In $BiFeO_3$, the competition between various exchange interactions manifests itself as non-collinear spin order, i.e., an incommensurate spin cycloid with a period of 64 nm.[5]

The experimentally known modification of bismuth ferrite crystallizes in the perovskite structure type (α) at standard conditions, with rhombohedral space group *R3c* (no. 161).[6-9] The residual porosity location, microstructure, size, grain growth habit and grain boundary geometry of the sintered specimen are very important factors in determining the electrical as well as magnetic properties of $BiFeO_3$. [10-13] Especially interesting are doped $BiFeO_3$ materials which can strongly affect the structure and properties of bismuth ferrite. In particular, various morphologies of Ho-substituted $BiFeO_3$ were recently fabricated including thin films [14-17], nanofilms [18], nanoparticles [19, 20], nanopowders [21, 22], nanocrystalline BFO [23], bulk and polycrystalline ceramics [24-27].

In this work, we investigated the influence of doping $BiFeO_3$ with Ho. Holmium serves as an interesting choice as it has the highest magnetic moment among the lanthanides series. In contrast to the so far investigated $BiFeO_3$ compounds doped with Ho, we have performed a detailed magnetic study which includes Zero field cooled (ZFC) and Field cooled (FC) curves above the Neel T_N temperature of the antiferromagnetic transition. Along with the magnetization measurements, we performed *ab initio* theoretical calculations. For utilizing the multiferroic properties of $BiFeO_3$ it is necessary to understand and control the spin cycloid in $BiFeO_3$.[28] Furthermore, the structure-property relationship has been investigated in great detail with respect to Ho doping in $BiFeO_3$ and additional perovskite structures have been predicted as well as their electronic and magnetic properties. This complete picture of synthesis, XRD and magnetic measurements combined with structure prediction and *ab intio* theoretical calculations gives valuable information about the influence of Ho substitution on magnetic behavior including the development of weak ferromagnetism and magnetic irreversibility.

2. Materials and methods

2.1. Synthesis and structural characterization of $Bi_{1-x}Ho_xFeO_3$ (x = 0.02, 0.05, 0.10) nanopowders

Nanocrystalline powders of $BiFeO_3$ and $Bi_{1-x}Ho_xFeO_3$ (x = 0.02, 0.05, 0.10) were made according to the hydrothermal method.[29, 30] The simple, low-cost and energy-saving hydrothermal method has advantages over the conventional methods. The chemical compounds used in this work were bismuth nitrate ($Bi(NO_3)_3$ x $5H_2O$), holmium nitrate ($Ho(NO_3)_3$ x $5H_2O$), iron nitrate ($Fe(NO_3)_3$ x $9H_2O$), and potassium hydroxide (KOH); all the chemicals were of an analytical grade. The mixtures of ($Bi(NO_3)_3$ x $5H_2O$), ($Ho(NO_3)_3$ x $5H_2O$) and ($Fe(NO_3)_3$ x $9H_2O$) were dissolved in 40 mL of 8 M KOH. The mixture was stirred vigorously for 30 min and transferred into an autoclave. The hydrothermal treatments were conducted under autogenous pressure at a temperature of 200 °C for 6 h. The produced powders were collected at the bottom of the autoclave after cooling to room temperature. The products were washed at least five times by repeated cycles of centrifugation in distilled water and dispersed in ethanol by sonicating for 60 min. The powders were obtained by evaporating ethanol in a mortar heated at 60 °C.

Structural characterization of the obtained powders was carried out using a Philips X-ray diffractometer (XRD) using a graphite monochromator using Cu-Kα radiation (wavelength λ =1.54 Å). The data for structural refinement was taken in the 2θ range of 10–90°, with a step width of 0.02° 2θ and 5 s per step. Refinement was performed using the X Pert HighScore Plus [31] computer program adopting the Rietveld calculation method.

2.2. Magnetic measurements

The magnetic behavior of the synthesized materials in the form of sintered pellets was investigated using a SQUID magnetometer equipped with an oven option. In this way, the temperature dependence of magnetization in a wide temperature interval (2-800 K) is obtained. Moreover, the combination of standard sample environment (2-400 K) and oven (300-800 K) is used especially in order to measure the true zero-field cooled (ZFC) and field-cooled (FC) magnetization curves. First, the sample is cooled down to 2K in zero field and measured in a field of 1000 Oe during heating up to 350K. Then the sample is moved from the standard plastic straw into the quartz tube oriented in the same direction and inserted into the oven installed within the sample space in the same magnetic field. Measurement is quickly continued from almost the same magnetic state at room temperature up to 800K. In this way, the full temperature range ZFC curve is obtained. Thereafter the measurement is continued in the same field of 1000 Oe from 800 K down to 350 K. Finally, the oven is uninstalled and the sample is transferred from the quartz tube into the plastic straw preserving direction to continue measurement from the same magnetic state. As the last step, the sample is measured down to 2K in the same field. Only in such a way, which is rarely found in the literature, the true and complete ZFC-FC curves are obtained, which is very important in order to correctly characterize the magnetic irreversibility in case of high-temperature magnetic transition.

Additionally, isothermal magnetic hysteresis curves at low temperatures (4 K) and room temperature (300 K) were measured.

2.3. Structure prediction and bond valence calculations

The main principles and methods of the crystal structure prediction and identification of structure candidates, especially including rare earth elements, have been given in detail elsewhere, [32-35] as well as the details about previous successful applications of these methods on perovskites. [36-38] In order to generate new structure candidates of Ho-doped $BiFeO_3$ perovskites we have used the Structure Prediction Diagnostic Software (SPuDS).[39] The SPuDS program is based on bond valence calculations and is used to predict the crystal structures of perovskites, including those distorted by tilting of symmetric octahedra or caused by Jahn-Teller distortions [36, 37, 39, 40]. The SPuDS software requires a minimum amount of input data: the composition ($Bi_{1-x}Ho_xFeO_3$, x = 0.02, 0.05, 0.10) and oxidation state of each ion (Bi^{+3}, Ho^{+3}, Fe^{+3}, O^{-2}). Afterward, structure optimization has been performed by restricting the octahedra to remain rigid during calculation, with six equivalent BX distances and all X-B-X angles equal to 90º. In this way, a full crystal structure can be generated from the size of the octahedron and the magnitude of the octahedral tilting distortion. Furthermore, SPuDS calculates the fractional position of each atom at each tilt angle step over a wide range of octahedral tilt angles.[39, 40]

The size of the octahedron and magnitude of the octahedral tilting distortion is calculated by using the bond valence model, S_{ij},

$$S_{ij} = e^{[(Rij-dij)/B]} \quad (1)$$

where d_{ij} is the cation-anion distance, the B parameter is empirically determined as a universal constant with a value of 0.37, and R_{ij} is empirically determined for each cation-anion pair, based on bond distances measurements.[39, 40]

The stability of the novel predicted perovskite structures is determined by comparing the calculated bond valence sums and the ideal formal valences. This quantity is known as the global instability index (GII) and it is calculated according to the Ho quantity in $BiFeO_3$ corresponding to the different Glazer tilt systems. The Goldschmidt tolerance factor [41] is another important value for investigating perovskite-related structures and is defined as a measure of the fit of the A-site cation to the cubic corner-sharing octahedral network.[39] SPuDS program uses both the ionic radii defined by Shannon [42] and the bond-valence parameters separately to calculate the tolerance factor (whenever possible). Theoretical determination and identification of the predicted structures were performed using the KPLOT program [43]. The symmetry of the predicted structures was analyzed with the algorithms SFND [44] and RGS [45], while duplicate structures were removed using the CMPZ algorithm [46]. The investigated structures were visualized using the VESTA code [47].

2.4. Ab initio structure and properties calculations

Calculations of the structural, electronic and magnetic properties have been performed using density functional theory (DFT) as implemented in the SIESTA code [48]. Periodic boundary

conditions have been used throughout the study. Calculation cells contain 30 atoms for the alpha phase, 40 atoms for beta, gamma, T1 and T2 crystals, while the crystal with R symmetry contains 60 atoms. One Ho atom is considered in each cell. We used the Perdew-Burke Ernzerhof (PBE) [49] exchange-correlation functional, norm-conserving Troullier-Martins pseudopotentials with partial core corrections, [50] and a double-ζ basis including polarization orbitals. The reciprocal space has been sampled by a fine Monkhorst-Pack mesh [51] of 8x8x4, 8x10x12, 12x12x12, 8x8x8, 8x12x12, and 8x12x12 k-points in the Brillouin zone (BZ) of the alpha, beta, gamma, R, T1 and T2 structures, respectively.

A high mesh cut-off energy of 700 Ry was used to determine the self-consistent density matrix. Geometries have been optimized using the conjugate gradient method [52] until none of the residual Hellmann-Feynman forces exceeded 0.04 eV/Å. Prior to the optimization of Ho-doped structures, bare Ho-free crystals were optimized. Lattice vectors were kept fixed since atomic forces and frequently density matrix could not converge in optimizations with varying lattice vectors. Since local functionals do not describe well some transition metals, including Fe, we utilized the DFT+U method and particularly its GGA+U flavor.[53-55] In all calculations we fixed the Hubbard U_{eff}=3.8eV for Fe 3d orbital and U_{eff}=0.95 for Fe 4s orbital, which was successfully used in our previous calculations. [38]

3. Results and discussion

3.1. X-Ray Powder Diffraction (XRPD) and Rietveld refinement of $Bi_{1-x}Ho_xFeO_3$ (x=0.02, 0.05, 0.10)

Samples doped with 2, 5 and 10 at. % of Ho, $Bi_{1-x}Ho_xFeO_3$ with x=0.02, 0.05, 0.10, were studied by powder X-ray diffraction and the data were refined by the Rietveld method. Rhombohedral *R3cH* structure [38] was taken as the starting structural model for the refinement. Ho atoms were introduced into the structural model assuming the substitution at the Bi atom site. For each sample, the occupancy of the site shared by Bi and Ho was fixed according to the starting synthesis conditions and was not refined. Refined patterns are shown in Figure 1 (a)-(c), while refined parameters are given in Table S1 (see supporting information).

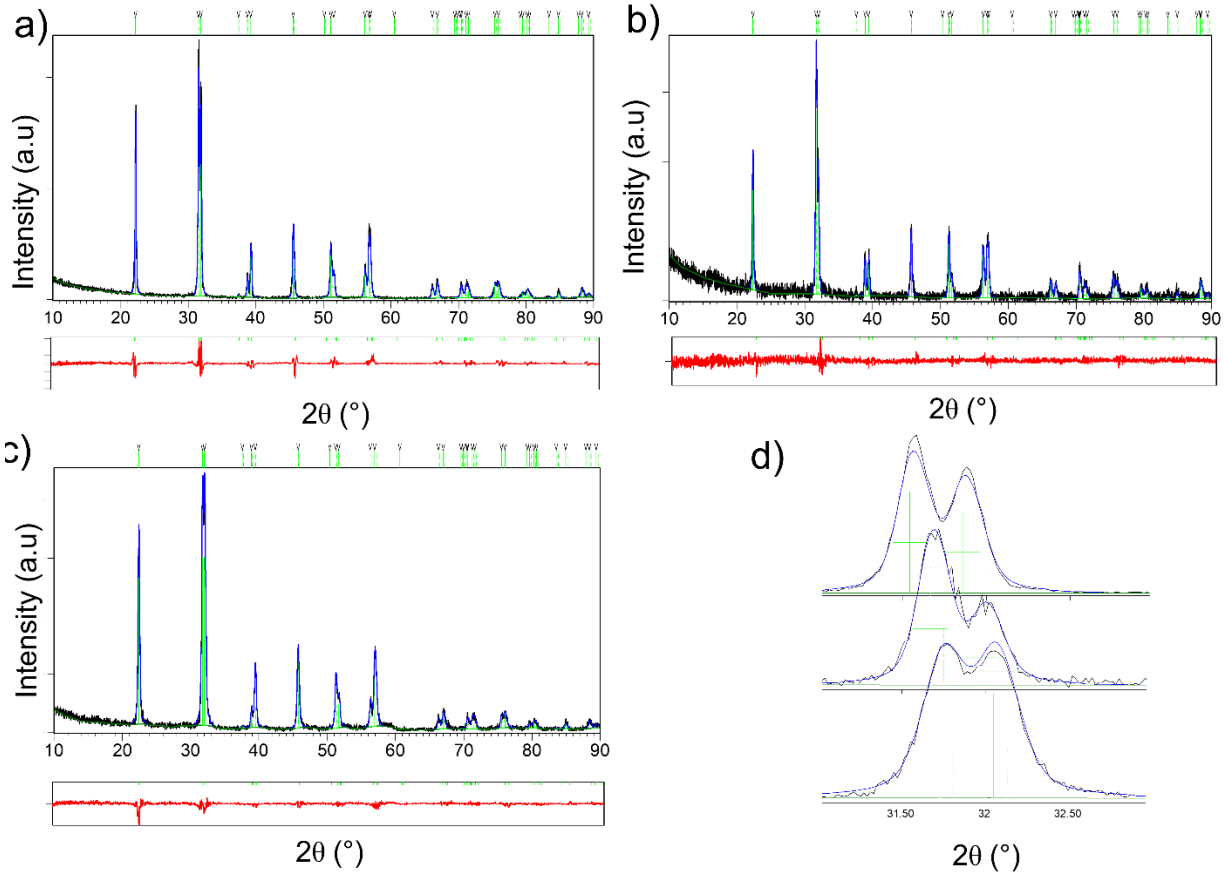

Figure 1. Rietveld refinement of the samples (a) BHFO-2, (b) BHFO-5 and (c) BHFO-10, having 2%, 5% and 10% of Ho in BFO, respectievly. The experimental curve is colored black whereas the refined one is colored blue. The difference between intensities is given at the bottom in red color. (d) The enlarged area between 31° and 33° 2Θ with diffraction lines (104) and (110).

Figure 1 (d) shows an evolution of the diffraction maxima (104) and (110) with the increase of the Ho content. These two maxima are shifting towards higher Bragg angles indicating that the lattice parameters decrease as the doping level of Ho increases. Furthermore, a slight change in the distance between the two maxima is observed, with the peaks getting closer to each other with the increase of the Ho content. This agrees with previous reports. [26, 56-61] which state that the resulting lattice distortion eventually suppresses the rhombohedral phase, transforming into the lower symmetric orthorhombic phase. This happens for *x*(Ho) larger than 10%. [20, 26]

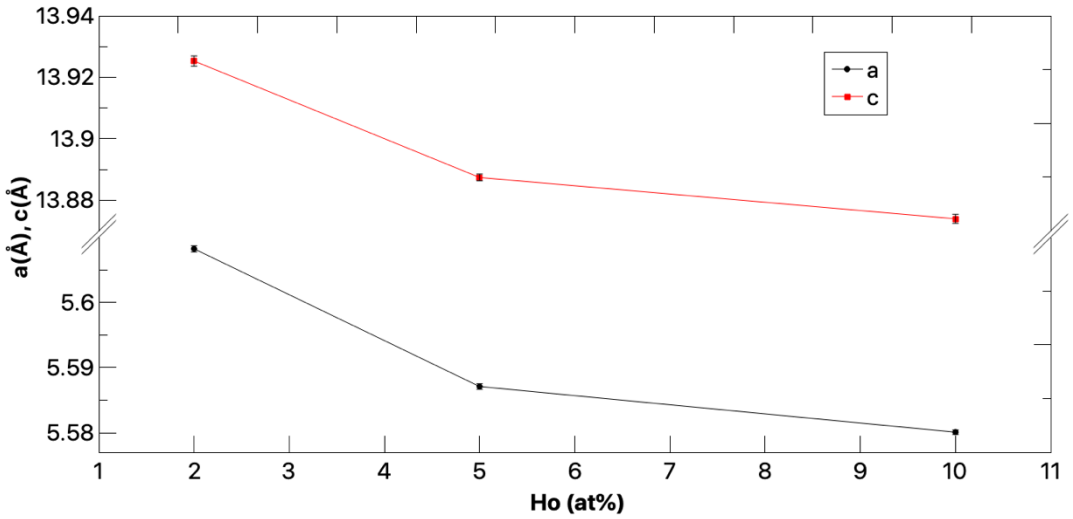

Figure 2. Lattice parameters *a* and *c* dependent on the Ho content in the alpha $BiFeO_3$.

The dependence of lattice parameters on the Ho content is shown in Figure 2, while numerical values of the lattice parameters are given in Table 1. It can be seen from the data above that the lattice parameters decrease with the introduction of the Ho atoms into the crystal lattice of $FeBiO_3$. This is to be fully expected as the ionic radius of Ho^{3+} (1.015 Å) is smaller than the ionic radius of Bi^{3+} (1.14 Å). An increase of the Ho content from 2% to 10% decreases lattice parameter *a* by 0.5% and lattice parameter *c* by 0.4%. Figure 3 shows the refined α-$BiFeO_3$ structure doped with holmium showing rhombohedral *R3cH* (no.161) space group.

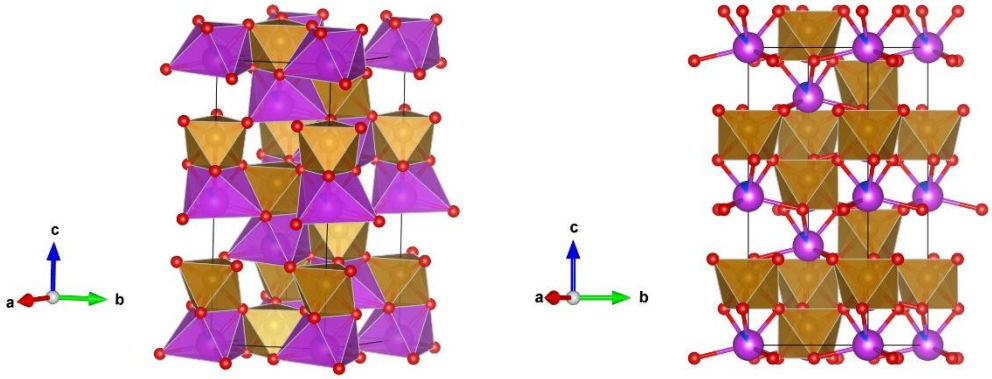

Figure 3. The refined α-$BiFeO_3$ structure doped with holmium in rhombohedral *R3cH* (no.161) space group: (a) polyhedra with sixfold coordination (CN=6) of the Bi/Ho atom by O atom and Fe by O are shown; (b) e.g. 10% of Ho doping on Bi atomic positions in the alpha phase.

.

Table 1. Lattice parameters of the samples with: 2% Ho (BHFO-2), 5% Ho (BHFO-5) and 10% Ho (BHFO-10) doping of $BiFeO_3$.

Sample	*a* (Å)	*c* (Å)
BHFO-2	5.6082(5)	13.9253(2)
BHFO-5	5.5870(4)	13.8873(1)
BHFO-10	5.5800(4)	13.8739(2)

3.2. Structure prediction of Ho-doped $BiFeO_3$ perovskites

Structure prediction in Ho-doped BFO was performed using bond valence calculations (BVC) and SPuDS code in order to find possible additional structure candidates besides experimentally observed α-$BiFeO_3$ perovskite structure. As a result, we have predicted 15 additional perovskite-related structure candidates in various chemical systems, depending on holmium doping in $BiFeO_3$. Table 2 shows calculated values of the global instability index (GII) and tilt system of the most promising predicted modifications in the $Bi_{0.98}Ho_{0.02}FeO_3$, $Bi_{0.95}Ho_{0.05}FeO_3$ and $Bi_{0.9}Ho_{0.1}FeO_3$ compound.

Table 2. Calculated values of the global instability index (GII) and tilt system of the most promising predicted modifications in the a) $Bi_{0.98}Ho_{0.02}FeO_3$; b) $Bi_{0.95}Ho_{0.05}FeO_3$; c) $Bi_{0.9}Ho_{0.1}FeO_3$ compound. Calculations were performed using the bond valence (BVC) method.

Composition	$Bi_{0.98}Ho_{0.02}FeO_3$		
Modification	**Space group**	**Tilt system**	**GII**
β-type	*Pnma*	$a^-b^+a^-$	0.03816
R-type	*R*-3*c*	$a^-a^-a^-$	0.04284
T_1-type	*P*4/*mbm*	$a^0a^0c^-$	0.08938
T_2-type	*I*4/*mcm*	$a^0a^0c^-$	0.08938
γ-type	*Pm*-3*m*	$a^0a^0a^0$	0.72910
	$Bi_{0.95}Ho_{0.05}FeO_3$		
β-type	*Pnma*	$a^-b^+a^-$	0.05815
R-type	*R*-3*c*	$a^-a^-a^-$	0.06113
T_1-type	*P*4/*mbm*	$a^0a^0c^-$	0.09992
T_2-type	*I*4/*mcm*	$a^0a^0c^-$	0.09992
γ-type	*Pm*-3*m*	$a^0a^0a^0$	0.73225
	$Bi_{0.9}Ho_{0.1}FeO_3$		
β-type	*Pnma*	$a^-b^+a^-$	0.08023
R-type	*R*-3*c*	$a^-a^-a^-$	0.08226
T_1-type	*P*4/*mbm*	a^0a^0c-	0.11480
T_2-type	*I*4/*mcm*	a^0a^0c-	0.11480
γ-type	*Pm*-3*m*	$a^0a^0a^0$	0.73746

The most stable $BiFeO_3$ perovskite structure with Ho-doping based on the GII criterion (Table 2), is the *β*-type in the space group *Pnma*, with GII ranging from 0.03816 to 0.08023 depending on the Ho content. This is in agreement with previous experimental and theoretical observations where the beta orthorhombic structure was found as a secondary phase in Ho-doped BFO. [20, 21, 26, 58-61] Predicted beta phase in the $Bi_{0.9}Ho_{0.1}FeO_3$ system (corresponding to 10% Ho-doping) is shown in Figure 4a.

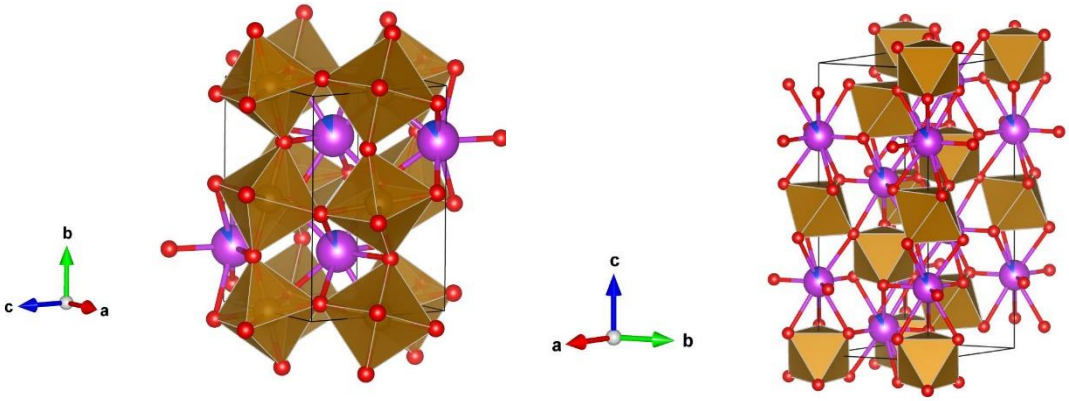

a) b)

Figure 4. Visualization of the predicted: a) β-type of structure in the space group *Pnma* (no.62) b) R-type in the rhombohedral *R-3c* (167) space group, in the $Bi_{0.9}Ho_{0.1}FeO_3$ system, corresponding to 10% of Ho doping in bismuth ferrite. Purple and blue balls correspond to Bi and Ho atoms, red atoms correspond to oxygen, while yellow atoms correspond to iron, represented by Fe-O octahedra in yellow color.

The next most stable predicted Ho-doped structure according to the GII index appears as R-type in the rhombohedral *R-3c* space group. The GII index of the R-type modification is close to the beta phase regardless of holmium content (Table 2). Moreover, R-type appears in the rhombohedral R-3c (no. 167) space group, structurally related to the experimentally observed alpha phase appearing in the rhombohedral R3c (no. 161) space group, making R-phase a strong structure candidate in Ho-doped BFO. In addition, previous experimental and theoretical data on pure $BiFeO_3$ show a high-temperature rhombohedral modification of $BiFeO_3$ [62-64], as our predicted R-phase. The predicted R-type in the $Bi_{0.9}Ho_{0.1}FeO_3$ system is shown in Figure 4b.

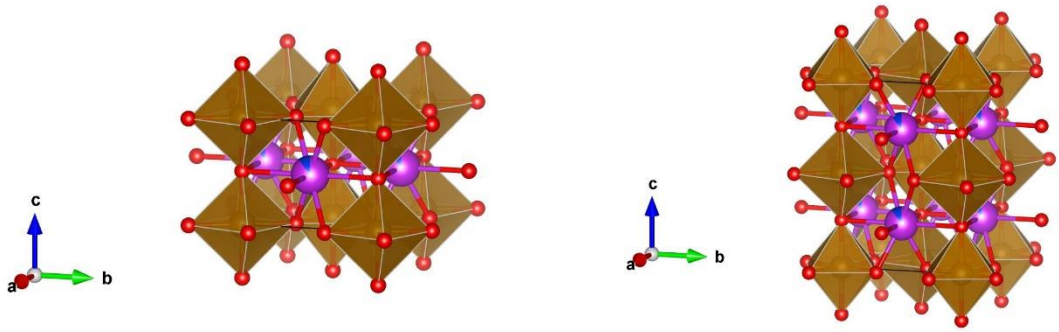

a) b)

Figure 5. Visualization of the predicted: a) T1-type structure appearing in the space group *P4/mbm* (no. 127); b) T2-type appearing in the *I4/mcm* (no. 140) space group, in the $Bi_{0.9}Ho_{0.1}FeO_3$ system. For colors see Figure 4.

Structure prediction using BVC calculations and GII index resulted in two additional tetragonal candidates, T1- and T2- type, which show the same value of GII index regardless of

Ho concentration in $BiFeO_3$ (Table 2). Both tetragonal T1 and T2 modifications are closely structurally related with T2 appearing as a polytype [32, 65] of T1 along the c-direction (Figures 5a and 5b). However, they are easily distinguishable by symmetry, where the T1 type appears in *P4/mbm* (no. 127) space group, and the T2 phase appears in *I4/mcm* (no. 140) space group. Alternative tetragonal phases have been previously reported in pristine $BiFeO_3$ at high temperatures,[66-68] as well as in our previous study,[38] supporting T1- and T2-types as very good structure candidates in Ho-doped BFO.

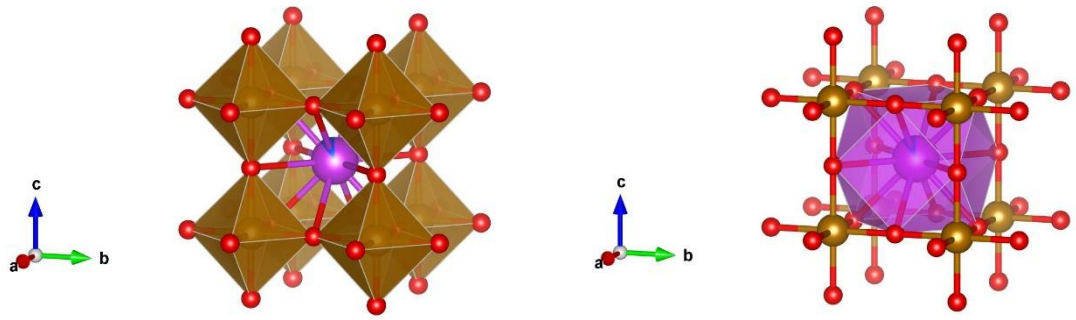

a) b)

Figure 6. Visualization of the predicted gamma phase in the $Bi_{0.9}Ho_{0.1}FeO_3$ system, corresponding to 10% of Ho doping in bismuth ferrite: a) six-fold coordination (CN=6) of the Fe atom by O forming perfect octahedra in cubic symmetry; b) twelve-fold coordination (CN=12) of the Bi/Ho atoms by O atom. For colors see Figure 4.

Finally, the γ-type modification is the structure candidate with the highest level of the GII index regardless of Ho concentration in bismuth ferrite (Table 2), but it also shows the highest cubic symmetry (*Pm*-3*m* (no. 221) space group). The Fe atoms are coordinated by six O atoms (CN=6), forming a perfect octahedron (Figure 6a), while Bi/Ho atoms are coordinated by twelve (CN=12) oxygen atoms, different from eight-fold coordination in previous tetragonal phases. (Figures 5 and 6). Similarly, as in previous cases, the gamma type has been found in the experiments and theoretical studies in pure $BiFeO_3$ at high temperatures, [63, 66, 69] and was found in our previous work on BFO, [38] indicating the possible existence of the gamma phase in the Ho-doped $BiFeO_3$. To further check for the structural stability of the predicted phases, and investigate their properties, we have performed *ab initio* structure optimization.

3.3. Ab initio structure optimization

Each of the predicted structure candidates generated using BVC calculations and SPuDs code, as well as equilibrium structures from experimental synthesis, were submitted to the *ab initio* local optimization using the conjugate gradient method. Hence, all calculations were done at absolute zero. In addition, all structures have been investigated for different magnetic ordering, ferromagnetic (FM) order and two antiferromagnetic orders (AFM1, AFM2). Since local functionals do not describe well some transition metals, including Fe, we utilized the DFT+U method and particularly its GGA+U flavor for local optimizations.[53-55] In all calculations we fixed the Hubbard U_{eff}=3.8eV for Fe 3d orbital and U_{eff}=0.95 for Fe 4s orbital, which was successfully used in our previous calculations. [38] Since in this reference, other software was utilized than the one in the present study, before the production work we found that these U_{eff} parameters produce band structure and DOS of bare $BiFeO_3$ very similar to those reported in the reference. We varied the U_{eff} of Ho 4f states (U_{eff} = 0.0, 2.5, 5.0, 7.5, 9.0) electronvolts in order to investigate the influence of Ueff on the electronic structure of the doped $BiFeO_3$ crystals.

Table 3. Calculated substitutional formation energies (eV/atom) of the alpha, beta, gamma, R, T1, and T2 type structures for the ferromagnetic (FM) and two antiferromagnetic orders (AFM1, AFM2). For the definition of x see in the text the considered chemical reaction. The energies are obtained using the DFT GGA+U method with fixed U_{eff} = 7.5eV for Ho 4f states. N/A means that data is not available as calculations could not converge.

	FM	**AFM1**	**AFM2**
alpha (x=1/6)	-0.257	-0.263	-0.248
beta (x=1/8)	-0.196	-0.199	-0.196
gamma (x=1/8)	-0.271	-0.255	-0.159
R (x=1/12)	N/A	-0.180	-0.186
T1 (x=1/8)	-0.258	-0.259	-0.241
T2 (x=1/8)	-0.228	-0.218	-0.198

To compare the stabilities of investigated structural types we present the substitutional formation energies of all optimized structures in Table 3. The substitutional energies were calculated using the following formula: $1/N_{at}$ [$E_{tot}(Bi_{1-x}Ho_xFeO_3)$ + x/2 $E_{tot}(Bi_2O_3)$ – $E_{tot}(BiFeO_3)$ – x/2 $E_{tot}(Ho_2O_3)$], where $E_{tot}(Y)$ is total energy of structure Y, x is the number of Bi atoms substituted by Ho atoms given per one Bi atom, N_{at} is the number of atoms per conventional unit cell for which DFT calculations were performed. Note that substitutional energies account for the difference in Bi:Fe:O:Ho stoichiometry of the investigated doped phases, i.e. the energies can be directly compared to obtain the relative plausibility of particular phases after Ho-doping. We considered the chemical reaction $BiFeO_3$ + x/2 Ho_2O_3 → $Bi_{1-x}Ho_xFeO_3$ + x/2 Bi_2O_3 for the calculations of substitutional formation energies which is simple and computationally inexpensive compared to the reaction that was essentially present in our experiments, and the exact atomic structures of nitrates involved in the experiments are not exactly known, whereas the exact atomic structures are necessary for DFT calculations. In order to have compatible and comparable values of the substitutional formation energies for different investigated structure types we fixed U_{eff} at 7.5eV in GGA+U calculations also for

Ho 4f states (as is the case for Fe states), since the total energies for most phases are minimized for this U_{eff} value. Data in Table 3 suggests that the ferromagnetic gamma phase is the most plausible Ho-doped phase, with substitutional formation energy of -0.271 eV/atom. However, it is by only 8 meV/atom smaller than the substitutional energy of the AFM1 alpha phase. Note that the alpha phase was observed in our experiments. Substitutional energies of the T1 phase in ferromagnetic and AFM1 magnetic orders are by only 5 meV/atoms and 4 meV/atom, respectively, larger than the substitutional energy of the AFM1 alpha phase. Hence, the T1 type structure is also relatively prospective among Ho-doped $BiFeO_3$ crystals, in contrast to other investigated phases in which substitutional energies deviate significantly more from the mentioned structures. Note that the beta phase found in experiments is a less stable phase according to our DFT study. This may be attributed to different chemical reactions used in the experiment and the one used for the calculation of substitutional energy from DFT calculations.

Table 4. Theoretical structural data of the $BiFeO_3$ perovskite modifications doped with 10% of Ho compared to experimental data when available.

Modification and space group	**Cell parameters(Å) and unit-cell volume (Å^3) in experiments**	**Theoretical cell parameters(Å) and unit-cell volume (Å^3)**
α-type *R3c* (no.161)	a=5.5800(4), c=13.8739(2) V=374.11	a=5.55, c=13.84 V=369.19
β-$Bi_{0.9}Ho_{0.1}FeO_3$ *Pnma* (no. 62)	a=5.588, b=7.816, c=5.377 V= 234.84*	a=5.60, b=7.76, c=5.39 V=233.93
R-$Bi_{0.9}Ho_{0.1}FeO_3$ *R*-3 *c* (no.167)	*N/A*	a=5.43, c=13.96 V=357.05
T_1-$Bi_{0.9}Ho_{0.1}FeO_3$ *P4/mbm* (no. 127)	*N/A*	a=5.35, c=4.03 V=115.45
T_2-$Bi_{0.9}Ho_{0.1}FeO_3$ *I4/mcm* (no. 140)	*N/A*	a=5.35, c=8.06 V=230.91
γ-$Bi_{0.9}Ho_{0.1}FeO_3$ *Pm*-3*m* (no. 221)	*N/A*	a=4.03 V=65.50

*ref [70]

A summary of calculated structural parameters of the most favorable $BiFeO_3$ perovskite structures in the $Bi_{0.9}Ho_{0.1}FeO_3$ system (corresponding to 10% of Ho doping in bismuth ferrite) compared to experimental data (when available) is presented in Table 4. Our theoretical results on the alpha phase correspond to a=5.55 Å and c=13.84 Å, which is in good agreement with our experimental results from the synthesis and Rietveld refinement (a=5.5800(4), c=13.8739(2), Table 4), and with previously reported data [56-58]. Similarly, our calculated beta type of structure concurs with experimentally observed modification for 10% of Ho-doping in $BiFeO_3$. [70] Other predicted structures are not yet synthesized in the Ho-doped BFO, however, structural data concur with the *ab inito* calculations from the pure $BiFeO_3$.[38] Full structural details of all predicted structures with 2%, 5% and 10% Ho doping can be found in the supporting information.

3.4. Magnetization study

Temperature dependence of magnetization measured as described in subsection 2.2 is shown in Figure 7a. The transition temperature for magnetic order does not change with the substitution, and amounts between 620-625 K (Figure 7b). The transition temperature of pure $BiFeO_3$ is also around 620 K, [10, 71] and the same transition temperature was observed with other substitutions, like with Gd, Nb, La, etc. [72-74]

The difference between the transition temperatures among these cases can be understood with chemical pressure induced with substitutions, [75] where it was found that the magnetic transition temperature increases at a rate of 0.66 K per 1% of Ca substitution. Performed substitution with Ho produces an influence of the same order. The absence of some larger change of magnetic transition temperature shows that the magnetic lattice of BFO is persistent to perturbations with substituted atoms and that the interactions which determine ordering temperature can not be perturbed by any of mentioned substitutions, that might have a reason in a very long period of magnetic cycloid which is known to be more than hundred times of crystal lattice unit. [76]

a)

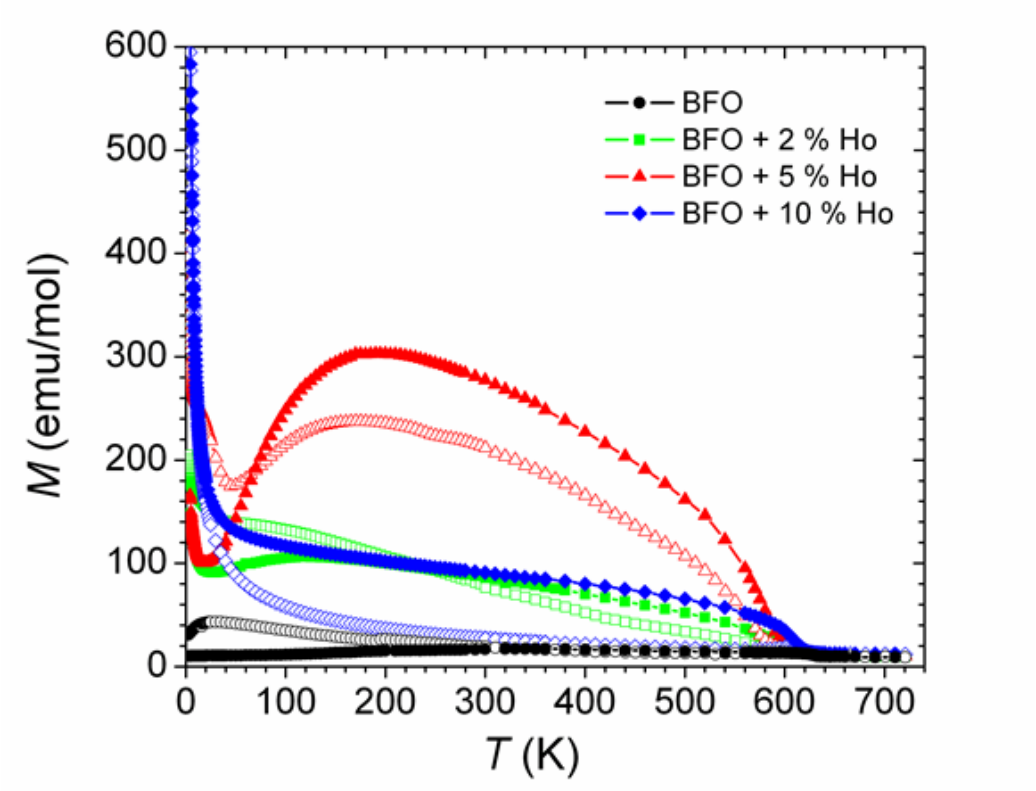

b)

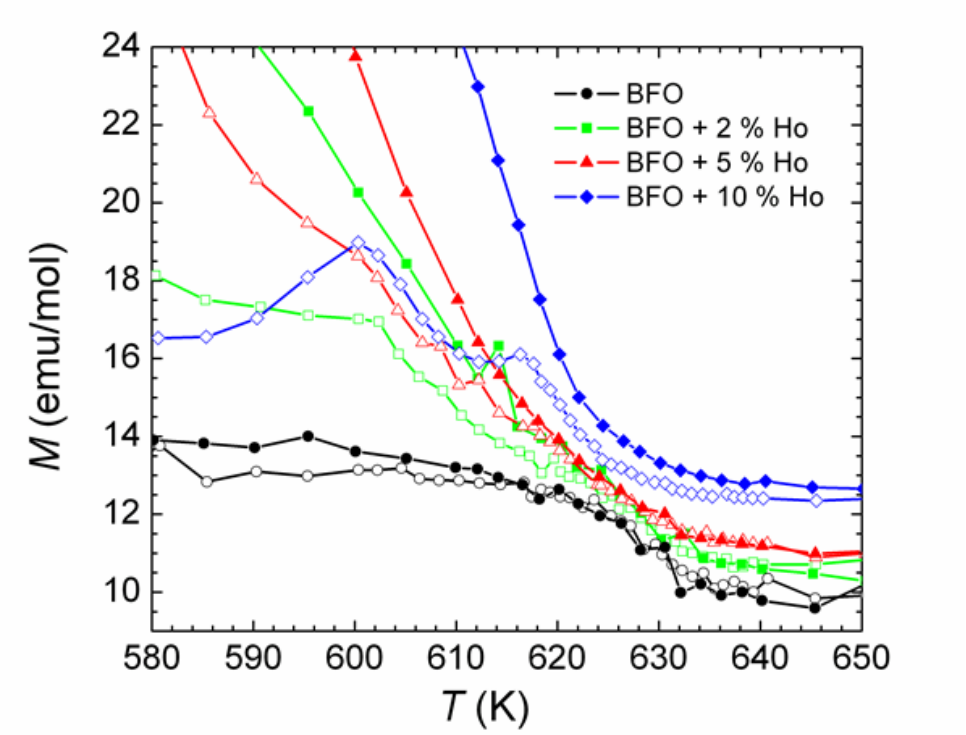

Figure 7. a) Temperature dependence of magnetization of pure $BiFeO_3$ and those substituted with 2, 5 and 10 % of Ho measured in a field of 1000 Oe. Splitting between the zero-field-cooled (ZFC) and field-cooled (FC) magnetization curves becomes more pronounced as the Ho concentration is increased, pointing to the development of weak ferromagnetic moment, which is usually connected with uncompensated spins or spin canting. b) The transition temperature region for magnetic order at around 620-625 K.

It is known that the nature of magnetic transition at T_N~620-625 K is antiferromagnetic. A well-observed peak at this temperature on ZFC M(T) confirms the antiferromagnetic nature of magnetic order for pure BFO. However, the FC M(T) curve below T_N is clearly separated from the ZFC one and increases with cooling below T_N, which is not a sign of the pure antiferromagnet. Instead, it can be concluded that the order is of a weak ferromagnetic kind. Indeed, weak ferromagnetism was obtained in theoretical calculations appearing as a result of Dzyaloshinskii-Moriya interactions. [77] Substituted samples actually do not have the peak in magnetization at the transition temperature, but both ZFC and FC curves increase with cooling below the ordering temperature, which is also a sign of weak ferromagnetic order. Both the ZFC-FC splitting and magnetization considerably increase with an increased amount of substitution, showing that weak ferromagnetic moment grows with the introduced defects, originating from the non-compensated magnetic moments due to the distortions of both the spin-cycloid order and the super-exchange bridges. Both distortions promote the additional spin-canting and increase the magnetization.

Another interesting phenomenon is the crossing of ZFC and FC curves. Generally, this crossing comes from the competition of the complex interactions between the magnetic sublattices as well as within the sublattices. A similar effect was demonstrated in holmium-iron-garnet. [78] This phenomenon was closely related to the magnetic structure of the Ho

sublattice which has transitioned from collinear to noncollinear spin-order and the development of a so-called magnetic umbrella structure. [79] This exotic magnetic structure was studied in detail in holmium-substituted YIG. [80] The Ho^{3+} ions with unquenched orbital angular momentum behave differently in different non-collinear sublattices, and the underlying mechanism is not understood in detail. However, it is worth noticing the similarity of the complex magnetic behavior in our case of substitution with holmium having an unquenched orbital momentum into BFO having a non-collinear spin structure. This might be the reason for the observed ZFC-FC crossing, but far from understood. It is interesting to note that the crossing temperature goes down with the increase of the substitution amount, which points to the interplay between complex interactions and thermal energy, which is not surprising in such cases. All of this is motivating for further experimental studies with microscopic magnetic probes (nuclear magnetic resonance, muon spin rotation, etc.) and with theoretical hard-work thermodynamic simulations embedded with non-collinear DFT.

The evolution of magnetic response to the magnetic field is further presented in the form of hysteresis loops in Figure 8. At low temperatures (4 K) the moment in the maximal field increases with the amount of substitution (Figure 8a). The loops are not saturated in a high field, but their tails seem paramagnetic-like, as was also observed previously with Gd substitution. The uncompensated moments are the main contributor to this magnetization value, since the pure BFO has very low magnetization, and they contribute to the M(T) at low temperatures in a paramagnetic-like manner. [72] A coercive field of the order of 1000 Oe is usual for substituted BFO being always a weak ferromagnet, but it is hard to compare exactly to other literature data, because of differences in microstructure which often determines magnetic hardness.

For the applicative side of these materials, it is more useful to look at the room-temperature hysteresis loops (Figure 8b). They also look typically as in weak ferromagnets: small hysteresis around zero and long straight lines for higher fields. The loop of the 10%Ho sample is surprisingly wide and with strong irreversibility up to the maximal measured field of 5T. Higher substitution (15%) is tried, but such an amount leads to the appearance of the secondary phases of metal oxides. The sample with 10%Ho is the highest achievable substitution which shows no presence of secondary phases as obtained by XRD analysis, but the observed wide hysteresis loop could suggest that some microscopic precipitates are formed being not visible in XRD patterns, which cause pinning of the domain walls and make this material as magnetically hard. Even the magnetization at 5T is comparable to some ordinary ferromagnets. This part of the study shows that it is possible to get some large magnetization from the weak ferromagnetic state, by 10% substitution with Ho.

a)

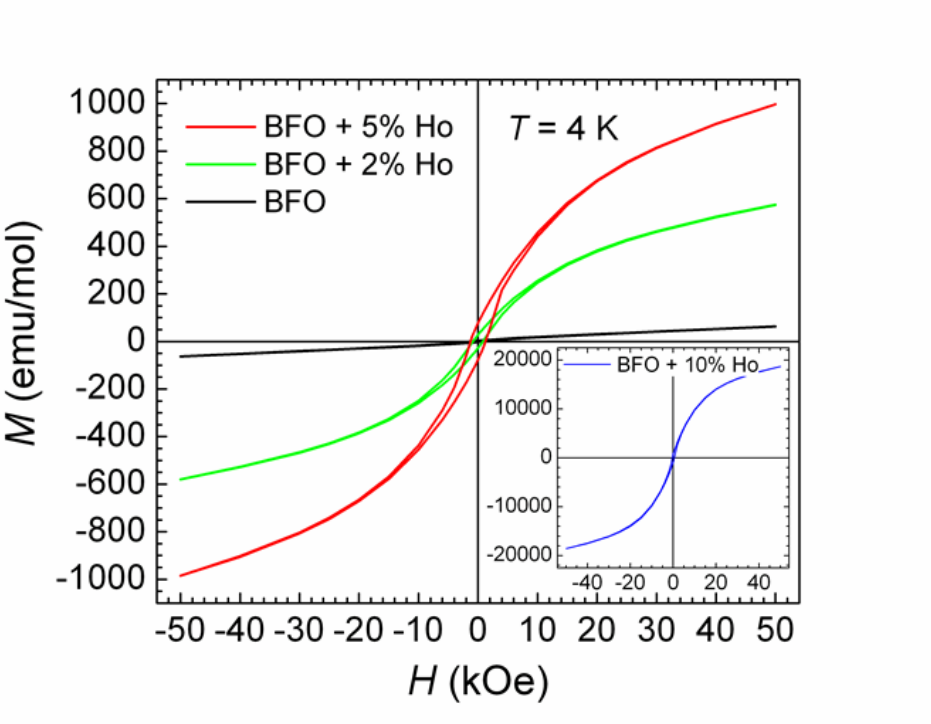

b)

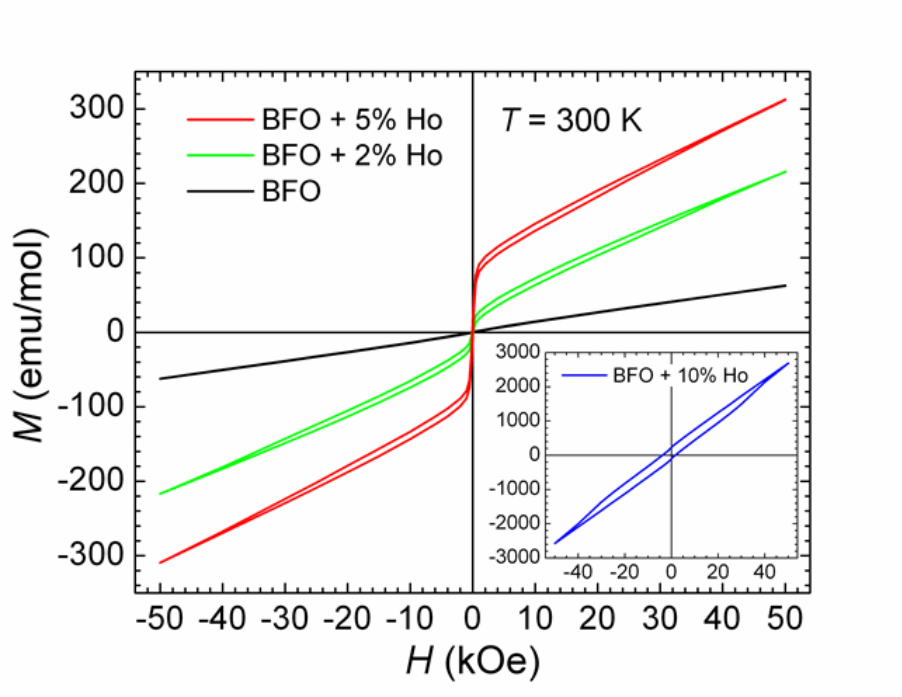

Figure 8. Magnetic hysteresis of pure $BiFeO_3$ and those substituted with 2, 5 and 10 % of Ho at: a) 4 K and b) 300 K.

3.5. *DFT calculations of electronic and magnetic properties*

Table 5. Summary of calculated electronic and magnetic properties of the Ho-doped BFO modifications using DFT. fm – ferromagnet, afm1 – antiferromagnet (A type), afm2 – antiferromagnet (G type). Data are derived from figures of electronic band structure and element-resolved density of states for all investigated phases, which are provided in the supplementary information.

Modification and mag. ordering		**type of el. str.**	**gap (eV)**	**gap character**	**dispersion of val. band**
alpha	fm	half-metal	0.80	direct	1.70
	afm1	half-metal	1.30	direct	1.60
	afm2	semiconductor	1.95	indirect	0.30
beta	fm	half-metal	0.50	direct	1.20
	afm1	semiconductor	0.2-1.7 (2)	direct	1.70
	afm2	semiconductor	2.0	direct	0.15
gamma	fm	semimetal	0.0		4.60
	afm1	semimetal	0.0		1.70
	afm2	semimetal	0.0		1.20
R	fm	(1)	(1)	(1)	(1)
	afm1	semiconductor	2.0	indirect	0.15
	afm2	semiconductor	2.0	indirect	0.30
T1	fm	half-metal	0.15	direct	1.20
	afm1	semiconductor	1.50	indirect	0.30
	afm2	semiconductor	1.0-1.4 (2)	direct	0.40
T2	fm	half-metal (valence)	0.20	direct	>0.2 (3)
	afm1	semicon.(U=0) metal (U=9)	0.0-0.7(2)	indirect	1.30
	afm2	semiconductor	0.90	indirect	1.40

(1) data are not available, DFT did not converge.
(2) gap changes with variation of Hubbard U_{eff} (used values 0.0, 2.5, 5.0, 7.5, and 9.0 eV).
(3) Below E_F-2eV hybridization with other states is too large hence the valence band is not distinguishable anymore.

As shown in Table 5, DFT predicts a rich variety of electronic structures among investigated Ho-doped BFO crystals, including half-metals, semiconductors, semimetals, and

metals. Such diversity eventually provides many possibilities for applications of these materials and further fundamental studies. In the ferromagnetic (FM) order in the calculation cells, all spins of Fe and Ho atoms are parallel. Two antiferromagnetic orders of Fe sublattice are considered: type A (AFM1, afm1 in table) and type G (AFM2, afm2 in table), which are determined by the spin texture of Fe sublattice. In the table, data obtained for U_{eff}=0 are shown. U_{eff} does not affect considerably these values except for T2 AFM1 for which it is semiconductor for U_{eff}=0 eV and metal for U_{eff}=9 eV. We neglected the presence of dopant states in the qualitative characterization of electronic structure type and determination of gap value. For example, in the alpha phase, we consider only electronic bands from Bi, Fe and O, which are all with spin-up character down to the energy E_F-0.8eV, making the phase half-metallic. Fermi energy in all crystals is placed in the valence band (close to its top), which can eventually be shifted into the gap with further doping or electrostatic gating.

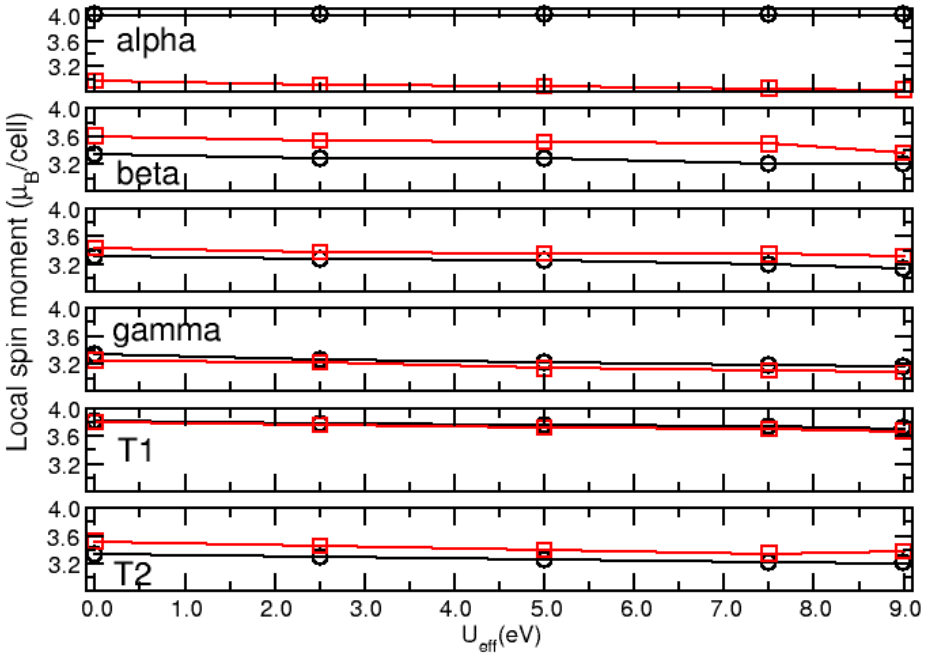

Figure 9. The local magnetic moment for AFM spin configurations. Black lines show data for AFM1 and red lines for AFM2.

The local magnetic moment in the AFM order originates primarily from the Ho dopant. In order to obtain macroscopic magnetization calculations with larger cells are necessary, which would give a possibility to investigate spin textures also on the Ho sublattice. However, since these larger calculations are very difficult to converge, we present here only the local magnetic moment of the cells with a single Ho atom. With such a setup Ho sublattice has an FM order. In the following figures atomic structure with spin texture, band structure and projected DOS are shown for select crystals. Black and red lines represent spin-up and spin-down states, respectively. As seen in Figure 9, Hubbard U_{eff} does not affect considerably the local magnetic moment. The effect of Hubbard U_{eff} in most cases is shifting of Ho 4f states, except for T2 AFM1 where other states are affected a bit too. Ho states around the Fermi level have small dispersion for all crystals, whereas dispersion enlarges a bit at larger binding

energies, which indicates the chemical bonding between Ho and surrounding O atoms at these energies.

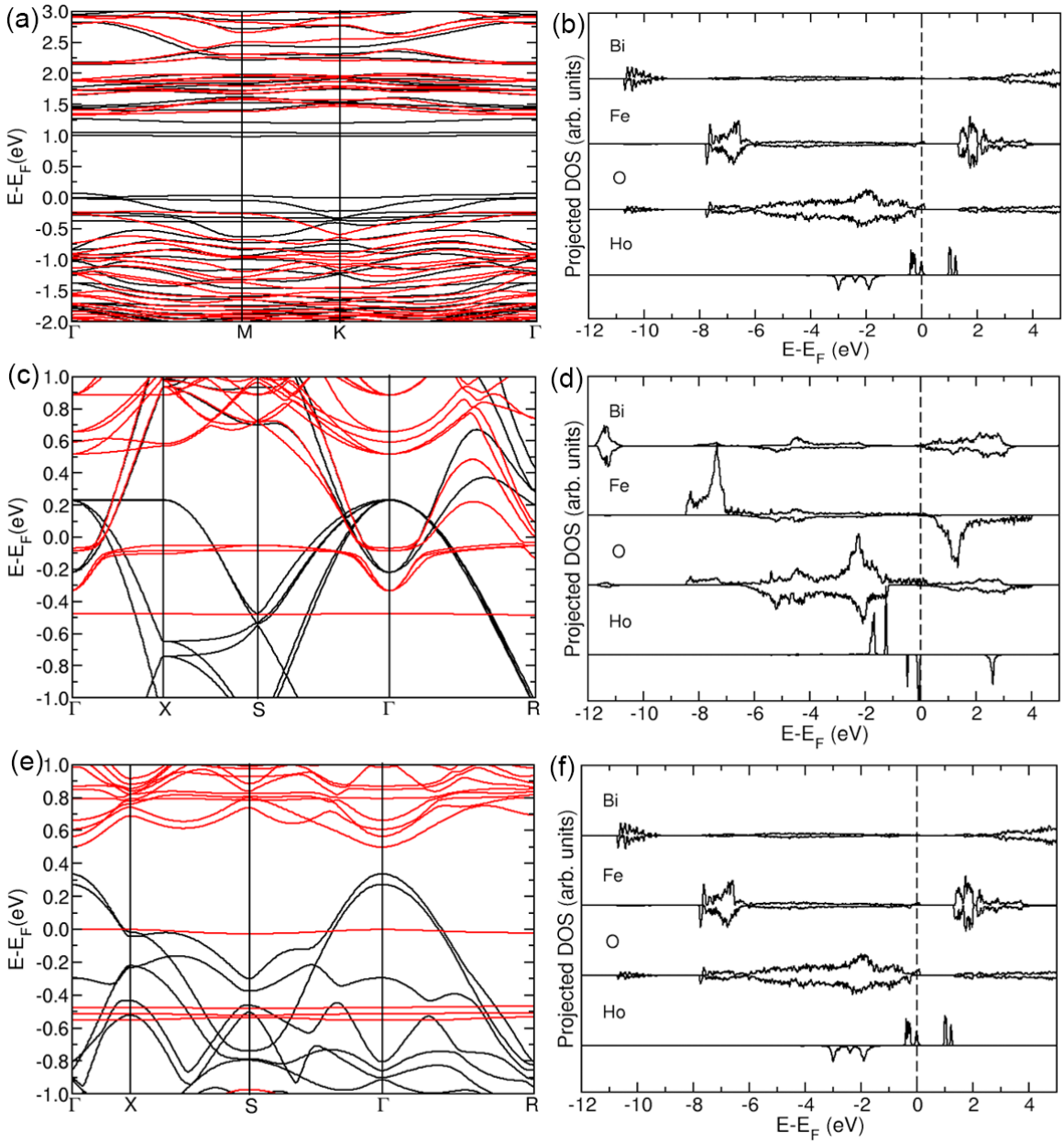

Figure 10. Electronic band structure of alpha AFM1 (a), gamma FM (c), T1 FM (e) and elements-resolved density of states of alpha AFM1 (b), gamma FM (d) and T1 FM (f) phases. Black lines present spin-up and red line spin-down bands. Mirrored graphs of the density of states correspond to spin-up and spin-down states.

The electronic structure and element-resolved density of state for Ho-doped BFO phases with the three smallest substitutional energies are shown in Figure 10. The Fermi level for these and all other investigated phases is always positioned in valence bands. The valence bands have Bi, Fe and O contributions in all investigated crystals. Some crystals have a very dispersive valence band with a dispersion larger than 1 eV, with the extreme of 4.6 eV in the band structure of gamma FM (Figures 10c and 10d). Gamma FM type structure appears as a

semimetal, as is shown also for gamma AFM1 and AFM2 (supporting figures S8 and S9). The Gamma FM phase may have a topological crossing of spin-up bands at the S k-point around 0.5 eV below the Fermi energy. However, this should be further investigated in future research. The large band dispersions in all of the calculated Ho-doped BFO modifications indicate the large conductance of these structures. The T1 FM has a relatively small gap with a large dispersion of valence and small dispersion of conduction bands (Figures 10e and 10f). This eventually opens a possibility to use these materials in electronic switches, where the conductive state may be switched on or off, for example, by shifting the Fermi level via electrostatic gating from the highly conductive valence band to/from the gap or the weakly conductive conduction band.

The alpha AFM1 (Figures 10a and 10b) has relatively flat both valence and conduction bands with a band gap of about 1 eV, indicating low electric conductance of the alpha AFM1 phase. The top of its valence band has a dominantly spin-up character, however, the spin-down character emerges already 0.25 eV below the Fermi energy. More interesting for application in spintronics are half-metals. Among other investigated phases half-metallic band structures are indicated for alpha FM, beta FM, T1 FM, and T2 FM (see Figures S1, S4, S11, and S14). Especially interesting are phases in which an electronic gap separates exclusively spin-up characterized valence and spin-down conduction bands, which are often considered for various spintronics applications. A typical example is the T1 FM phase, as shown in Figures 10e and 10f. Further electronic and magnetic properties of the alpha, beta, gamma, R-, T1- and T2- type structures, with their calculated band structures and DOS in the FM, AFM1 and AFM2 magnetic ordering are presented in the supporting information.

4. Conclusions

A multidisciplinary study has been performed to investigate the influence of Bi/Ho substitution in $BiFeO_3$. Nanocrystalline powders of $Bi_{1-x}Ho_xFeO_3$ with x=0.02, 0.05, 0.10, were synthesized using the hydrothermal method. Structure prediction in Ho-doped BFO was performed using bond valence calculations to find possible additional structure candidates besides experimentally observed α-$BiFeO_3$ perovskite structure. As a result, we have predicted the α-, β-,γ-, R-, T1, and T2 structure types in various Ho-doped BFO systems. Each of the predicted structure candidates generated using BVC calculations, as well as equilibrium structures from experimental synthesis, were submitted to the *ab initio* local optimization. In addition, all structure candidates have been investigated for different magnetic ordering, ferromagnetic (FM) and two antiferromagnetic orders (AFM1, AFM2). The DFT optimizations show that the most likely phases of BFO upon Ho-doping are gamma FM, alpha AFM1 and T1 FM and AFM1. Moreover, present DFT results are in good agreement with our experimental results from the synthesis and with previously reported data when existing.

Electronic and magnetic properties of synthesized and predicted perovskite structures have been studied as a function of the Ho-substitution. The magnetic behavior of the synthesized materials was investigated using a SQUID magnetometer equipped with an oven option that gave temperature dependence of magnetization in a wide temperature interval of 2 – 800 K. This full temperature range measurement showed as exceptionally important because

only in this way the true zero-field cooled (ZFC) and field-cooled (FC) curves were obtained, with the correct picture of the thermal irreversibility. The transition temperature for magnetic order does not change with the substitution considerably, staying between 620-625 K. Observed behavior of the temperature dependence of magnetization confirmed the weak ferromagnetic state of the substituted $BiFeO_3$ and showed the enhancement of the weak ferromagnetic moment with increased substitution. Also, the magnetic hysteresis loops of pure $BiFeO_3$ and those substituted with 2, 5 and 10 % of Ho at both 4 K and 300 K exhibited higher magnetic response with increased substitution, having the origin in the higher magnetic moment of holmium ion, and more important in the influence of substitution on the interactions and local magnetic order around the substituents. Furthermore, the widening of the hysteresis loops with substitution has its origin in increased thermal irreversibility coming from also from the influence of holmium onto the magnetic lattice distortions. For the applicative side of these materials, the room-temperature hysteresis loops also look typically as in weak ferromagnets, and with increased substitution, they develop considerable magnetic hardness.

Present *ab initio* calculations based on DFT predict a rich variety of electronic structures among investigated Ho-doped BFO perovskite modifications, including half-metals, semiconductors, semimetals, and metals, and such diversity eventually provides many possibilities for applications and further fundamental studies. Alpha FM, beta AFM1, T1 FM and T2 FM have relatively small gaps with large dispersions of valence and small dispersion of conduction bands. This eventually opens the possibility to use these materials in electronic switches. Even more interesting for application in spintronics are half-metals, alpha FM and AFM1, beta FM, T1 FM, and T2 FM. Semimetals, which include the gamma structure with any spin texture, provide further opportunities to investigate possible nontrivial topologies in their band structures. In most of the investigated structures, a flat Ho state is positioned at the Fermi level, which originates a large DOS. Large DOS at the Fermi level may cause many instabilities and corresponding physical phenomena, like (spin) charge density waves and superconductivity. The prosperous diversity of electronic and magnetic properties and more importantly the possibility of their tuning by doping inspire us and hopefully the community for a deeper research of individual phases and their properties.

Acknowledgments

This work was supported by the Croatian Science Foundation, Zagreb, Croatia [project UIP-2014-09-8276]; and by the Ministry of Science, Technological Development and Innovation of the Republic of Serbia, Belgrade, Serbia [Grant nos. 451-03-68/2022-14/200017, 1702313 and 0402311]. M.Č. acknowledges the support of the European Research Council (ERC Consolidator Grant No.725521) and Bilateral Project Between Serbia and Austria (OeAD-GmbH-Project No. RS 24/2022) 337-00-577/2021-09/6. We acknowledge the support from the COST Action CA17123 - Ultrafast opto-magneto-electronics for non-dissipative information technology (MAGNETOFON). M.Č., F.T., T.K., Ž.S. and D.P. acknowledge the support of project CeNIKS, co-financed by the Croatian Government and the EU through the European Regional Development Fund: Competitiveness and Cohesion Operational Programme (grant KK.01.1.1.02.0013). I. Popov acknowledges the financial support from the Ministry for

Education, Science and technological development of the Republic of Serbia, contract with the Institute for Multi-disciplinary Research, University of Belgrade 451-03-68/2022-14/200053. DFT calculations are performed using computational resources at the Center of Surface and Nanoanalytics, Johannes Kepler University, Linz, Austria. We are grateful to Prof. Kurt Hingerl for providing the necessary computational resources at JKU. We are grateful to Andrey Enyashin from the Institute of Mathematics and Computer Science, Ural Federal University, Yekaterinburg, Russia, for enlightening discussions.

Author contributions

M.C., D.Z., I.P. and D.P. conceived the idea; M.C. performed the synthesis of the $Bi_{1-x}Ho_xFeO_3$ (x = 0.02, 0.05, 0.10) nanopowders; XRD characterization, analysis, and Rietveld refinement have been performed by T.K. and Z.S.; SQUID measurements and magnetization study were carried out by F.T. and D.P., Structure prediction and BVC calculations were carried out by D.Z.; The ab initio structure optimizations and DFT calculations were performed by I.P.; All authors contributed to the discussion and writing of the paper. All authors have read and agreed to the published version of the manuscript.

Declaration of Competing Interest

The authors declare that they have no known competing financial interests or personal relationships that could have appeared to influence the work reported in this paper.

Supplementary materials

Supplementary material associated with this article can be found, in the online version.

References

[1] N.A. Spaldin, R. Ramesh, Advances in magnetoelectric multiferroics, Nature Materials, 18 (2019) 203-212.
[2] M. Bibes, A. Barthélémy, Towards a magnetoelectric memory, Nature Materials, 7 (2008) 425-426.
[3] H. Béa, M. Gajek, M. Bibes, A. Barthélémy, Spintronics with multiferroics, Journal of Physics: Condensed Matter, 20 (2008) 434221.
[4] J. Liu, M. Niu, L. Wang, C. Peng, D. Xu, Effect of tuning A/B substitutions on multiferroic characteristics of BiFeO3-based ternary system ceramics, Journal of Magnetism and Magnetic Materials, 510 (2020) 166928.
[5] S.R. Burns, D. Sando, B. Xu, B. Dupé, L. Russell, G. Deng, R. Clements, O.H.C. Paull, J. Seidel, L. Bellaiche, N. Valanoor, C. Ulrich, Expansion of the spin cycloid in multiferroic BiFeO3 thin films, npj Quantum Materials, 4 (2019) 18.
[6] J.M. Moreau, C. Michel, R. Gerson, W.J. James, Ferroelectric BiFeO3 X-ray and neutron diffraction study, Journal of Physics and Chemistry of Solids, 32 (1971) 1315-1320.
[7] F. Kubel, H. Schmid, Structure of a ferroelectric and ferroelastic monodomain crystal of the perovskite BiFeO3, Acta Crystallographica Section B, 46 (1990) 698-702.
[8] J. Wang, J.B. Neaton, H. Zheng, V. Nagarajan, S.B. Ogale, B. Liu, D. Viehland, V. Vaithyanathan, D.G. Schlom, U.V. Waghmare, N.A. Spaldin, K.M. Rabe, M. Wuttig, R. Ramesh, Epitaxial BiFeO3 Multiferroic Thin Film Heterostructures, Science, 299 (2003) 1719-1722.

[9] H. Feng, Magnetism and electronic properties of BiFeO3 under lower pressure, Journal of Magnetism and Magnetic Materials, 322 (2010) 3755-3759.
[10] G. Catalan, J.F. Scott, Physics and Applications of Bismuth Ferrite, Advanced Materials, 21 (2009) 2463-2485.
[11] L.W. Martin, S.P. Crane, Y.H. Chu, M.B. Holcomb, M. Gajek, M. Huijben, C.H. Yang, N. Balke, R. Ramesh, Multiferroics and magnetoelectrics: thin films and nanostructures, Journal of Physics: Condensed Matter, 20 (2008) 434220.
[12] J. Wu, Z. Fan, D. Xiao, J. Zhu, J. Wang, Multiferroic bismuth ferrite-based materials for multifunctional applications: Ceramic bulks, thin films and nanostructures, Progress in Materials Science, 84 (2016) 335-402.
[13] J.-G. Park, M.D. Le, J. Jeong, S. Lee, Structure and spin dynamics of multiferroic BiFeO3, Journal of Physics: Condensed Matter, 26 (2014) 433202.
[14] Y. Wang, Y. Wang, M. Wei, J. Zhang, Y. Zhang, Role of Ho Doping in Magnetization Mechanism of BiFeO3 Thin Films, Journal of Superconductivity and Novel Magnetism, 32 (2019) 3495-3501.
[15] Y.Q. Liu, Y.J. Wang, J. Zhang, M. Gao, Y.J. Zhang, M.B. Wei, J.H. Yang, Effect of Ho substitution on structure and magnetic property of BiFeO3 prepared by sol–gel method, Materials Science in Semiconductor Processing, 40 (2015) 787-795.
[16] S. Sharif, G. Murtaza, T. Meydan, P.I. Williams, J. Cuenca, S.H. Hashimdeen, F. Shaheen, R. Ahmad, Structural, surface morphology, dielectric and magnetic properties of holmium doped BiFeO3 thin films prepared by pulsed laser deposition, Thin Solid Films, 662 (2018) 83-89.
[17] P. Hou, B. Liu, Z. Guo, P. Zhou, B. Wang, L. Zhao, Effect of Ho doping on the crystal structure, surface morphology and magnetic property of BiFeO3 thin films prepared via the sol-gel technology, Journal of Alloys and Compounds, 775 (2019) 59-62.
[18] Q. Yun, A. Bai, S. Zhao, Lattice distortion of holmium doped bismuth ferrite nanofilms, Journal of Rare Earths, 32 (2014) 884-889.
[19] M.R. Islam, M.A. Zubair, R.H. Galib, M.S.B. Hoque, J.A. Tomko, K. Aryana, A.K. Basak, P.E. Hopkins, Vacancy-Induced Temperature-Dependent Thermal and Magnetic Properties of Holmium-Substituted Bismuth Ferrite Nanoparticle Compacts, ACS Applied Materials & Interfaces, 14 (2022) 25886-25897.
[20] S. Chaturvedi, R. Bag, V. Sathe, S. Kulkarni, S. Singh, Holmium induced enhanced functionality at room temperature and structural phase transition at high temperature in bismuth ferrite nanoparticles, Journal of Materials Chemistry C, 4 (2016) 780-792.
[21] B. Stojadinović, Z. Dohčević-Mitrović, D. Stepanenko, M. Rosić, I. Petronijević, N. Tasić, N. Ilić, B. Matović, B. Stojanović, Dielectric and ferroelectric properties of Ho-doped BiFeO3 nanopowders across the structural phase transition, Ceramics International, 43 (2017) 16531-16538.
[22] D. Kuang, F. Yang, W. Wang, Z. Yang, Effects of Ho3+ and transition metal ion doping on optical and magnetic properties of BiFeO3 nanopowders, Journal of Materials Science: Materials in Electronics, 29 (2018) 4041-4047.
[23] P. Thakuria, P.A. Joy, High room temperature ferromagnetic moment of Ho substituted nanocrystalline BiFeO3, Applied Physics Letters, 97 (2010) 162504.
[24] N. Jeon, D. Rout, I.W. Kim, S.-J.L. Kang, Enhanced multiferroic properties of single-phase BiFeO3 bulk ceramics by Ho doping, Applied Physics Letters, 98 (2011) 072901.
[25] S.K. Pradhan, J. Das, P.P. Rout, V.R. Mohanta, S.K. Das, S. Samantray, D.R. Sahu, J.L. Huang, S. Verma, B.K. Roul, Effect of holmium substitution for the improvement of multiferroic properties of BiFeO3, Journal of Physics and Chemistry of Solids, 71 (2010) 1557-1564.
[26] N. Van Minh, N. Gia Quan, Structural, optical and electromagnetic properties of Bi1−xHoxFeO3 multiferroic materials, Journal of Alloys and Compounds, 509 (2011) 2663-2666.
[27] M. Muneeswaran, S.H. Lee, D.H. Kim, B.S. Jung, S.H. Chang, J.-W. Jang, B.C. Choi, J.H. Jeong, N.V. Giridharan, C. Venkateswaran, Structural, vibrational, and enhanced magneto-electric coupling in Ho-substituted BiFeO3, Journal of Alloys and Compounds, 750 (2018) 276-285.

[28] A. Haykal, J. Fischer, W. Akhtar, J.Y. Chauleau, D. Sando, A. Finco, F. Godel, Y.A. Birkhölzer, C. Carrétéro, N. Jaouen, M. Bibes, M. Viret, S. Fusil, V. Jacques, V. Garcia, Antiferromagnetic textures in BiFeO3 controlled by strain and electric field, Nature Communications, 11 (2020) 1704.
[29] J. Maletaškić, M. Čebela, M.P. Đorđević, D. Kozlenko, S. Kichanov, M. Mitrić, B. Matović, Combined magnetic and structural characterization of hidrothermal bismuth ferrite (Bifeo3) nanoparticles, Science of Sintering, 51 (2019) 71-79.
[30] M. Cebela, B. Jankovic, R. Hercigonja, M.J. Lukic, Z. Dohcevic-Mitrovic, D. Milivojevic, B. Matovic, Comprehensive characterization of BiFeO3 powder synthesized by the hydrothermal procedure, Processing and Application of Ceramics, 10 (2016) 201-208.
[31] T. Degen, M. Sadki, E. Bron, U. König, G. Nénert, The HighScore suite, Powder Diffraction, 29 (2014) S13-S18.
[32] D. Zagorac, J.C. Schön, Energy landscapes of pure and doped ZnO: from bulk crystals to nanostructures, Frontiers of Nanoscience2022, pp. 151-193.
[33] J. Zagorac, J.C. Schön, B. Matović, T. Škundrić, D. Zagorac, Predicting Feasible Modifications of Ce2ON2 Using a Combination of Global Optimization and Data Mining, Journal of Phase Equilibria and Diffusion, 41 (2020) 538-549.
[34] C. Buyer, H. Grossholz, S. Wolf, D. Zagorac, J. Zagorac, J.C. Schön, T. Schleid, Crystal-Structure Prediction and Experimental Investigation of the Polymorphic Lanthanum Fluoride Selenides LaFSe and La2F4Se, Crystal Growth & Design, 22 (2022) 7133–7142.
[35] M. Pejić, D. Zagorac, J. Zagorac, B. Matović, J.C. Schön, Structure prediction via global energy landscape exploration of the ternary rare-earth compound LaOI, Zeitschrift für anorganische und allgemeine Chemie, 648 (2022) e202200308.
[36] J. Zagorac, D. Zagorac, A. Zarubica, J.C. Schön, K. Djuris, B. Matovic, Prediction of possible CaMnO3 modifications using an ab initio minimization data-mining approach, Acta Crystallographica Section B: Structural Science, Crystal Engineering and Materials, 70 (2014) 809-819.
[37] M. Rosić, D. Zagorac, D. Milivojević, N. Paunović, J. Zagorac, Z. Dohčević-Mitrović, B. Matović, Theoretical and experimental study of octahedral tilting of Ca1-xGdxMnO3 (x = 0.05, 0.1, 0.15, 0.2) nanometric powders, Journal of Alloys and Compounds, 678 (2016) 219-227.
[38] M. Čebela, D. Zagorac, K. Batalović, J. Radaković, B. Stojadinović, V. Spasojević, R. Hercigonja, BiFeO3 perovskites: A multidisciplinary approach to multiferroics, Ceramics International, 43 (2017) 1256-1264.
[39] M.W. Lufaso, P.M. Woodward, Prediction of the crystal structures of perovskites using the software program SPuDS, Acta Crystallographica Section B, 57 (2001) 725-738.
[40] M.W. Lufaso, P.M. Woodward, Jahn-Teller distortions, cation ordering and octahedral tilting in perovskites, Acta Crystallographica Section B, 60 (2004) 10-20.
[41] V.M. Goldschmidt, Die Gesetze der Krystallochemie, Naturwissenschaften, 14 (1926) 477-485.
[42] R. Shannon, Revised effective ionic radii and systematic studies of interatomic distances in halides and chalcogenides, Acta Crystallographica Section A, 32 (1976) 751-767.
[43] R. Hundt, KPLOT: A Program for Plotting and Analysing Crystal Structures, Technicum Scientific Publishing, Stuttgart, 2016.
[44] R. Hundt, J.C. Schön, A. Hannemann, M. Jansen, Determination of symmetries and idealized cell parameters for simulated structures, Journal of Applied Crystallography, 32 (1999) 413-416.
[45] A. Hannemann, R. Hundt, J.C. Schön, M. Jansen, A New Algorithm for Space-Group Determination, Journal of Applied Crystallography, 31 (1998) 922-928.
[46] R. Hundt, J.C. Schön, M. Jansen, CMPZ - an algorithm for the efficient comparison of periodic structures, Journal of Applied Crystallography, 39 (2006) 6-16.
[47] K. Momma, F. Izumi, VESTA 3 for three-dimensional visualization of crystal, volumetric and morphology data, Journal of Applied Crystallography, 44 (2011) 1272-1276.
[48] E. Artacho, E. Anglada, O. Diéguez, J.D. Gale, A. García, J. Junquera, R.M. Martin, P. Ordejón, J.M. Pruneda, D. Sánchez-Portal, J.M. Soler, The SIESTA method; developments and applicability, Journal of Physics: Condensed Matter, 20 (2008) 064208.

[49] J.P. Perdew, K. Burke, M. Ernzerhof, Generalized Gradient Approximation Made Simple, Physical Review Letters, 77 (1996) 3865-3868.
[50] N. Troullier, J.L. Martins, Efficient pseudopotentials for plane-wave calculations, Physical Review B, 43 (1991) 1993-2006.
[51] H.J. Monkhorst, J.D. Pack, Special points for Brillouin-zone integrations, Physical Review B, 13 (1976) 5188-5192.
[52] M.R. Hestenes, E. Stiefel, Methods of conjugate gradients for solving linear systems, J Res NIST, 49 (1952) 409--436.
[53] A.I. Liechtenstein, V.I. Anisimov, J. Zaanen, Density-functional theory and strong interactions: Orbital ordering in Mott-Hubbard insulators, Physical Review B, 52 (1995) R5467-R5470.
[54] V.I. Anisimov, J. Zaanen, O.K. Andersen, Band theory and Mott insulators: Hubbard U instead of Stoner I, Physical Review B, 44 (1991) 943-954.
[55] I.A. Vladimir, F. Aryasetiawan, A.I. Lichtenstein, First-principles calculations of the electronic structure and spectra of strongly correlated systems: the LDA+ U method, Journal of Physics: Condensed Matter, 9 (1997) 767.
[56] P. Suresh, P.D. Babu, S. Srinath, Effect of Ho substitution on structure and magnetic properties of BiFeO3, Journal of Applied Physics, 115 (2014) 17D905.
[57] S. Chaturvedi, M.M. Shirolkar, R. Rajendra, S. Singh, N. Ballav, S. Kulkarni, Coercivity and exchange bias of bismuth ferrite nanoparticles isolated by polymer coating, Journal of Applied Physics, 115 (2014) 123906.
[58] S. Chaturvedi, I. Sarkar, M.M. Shirolkar, U.-S. Jeng, Y.-Q. Yeh, R. Rajendra, N. Ballav, S. Kulkarni, Probing bismuth ferrite nanoparticles by hard x-ray photoemission: Anomalous occurrence of metallic bismuth, Applied Physics Letters, 105 (2014) 102910.
[59] G.L. Song, G.J. Ma, J. Su, T.X. Wang, H.Y. Yang, F.G. Chang, Effect of Ho3+doping on the electric, dielectric, ferromagnetic properties and TC of BiFeO3 ceramics, Ceramics International, 40 (2014) 3579-3587.
[60] Y. Wu, J.-g. Wan, C. Huang, Y. Weng, S. Zhao, J.-m. Liu, G. Wang, Strong magnetoelectric coupling in multiferroic BiFeO3–Pb(Zr0.52Ti0.48)O3 composite films derived from electrophoretic deposition, Applied Physics Letters, 93 (2008) 192915.
[61] Z.-L. Hou, H.-F. Zhou, L.-B. Kong, H.-B. Jin, X. Qi, M.-S. Cao, Enhanced ferromagnetism and microwave absorption properties of BiFeO3 nanocrystals with Ho substitution, Materials Letters, 84 (2012) 110-113.
[62] S.M. Selbach, T. Tybell, M.-A. Einarsrud, T. Grande, The Ferroic Phase Transitions of BiFeO3, Advanced Materials, 20 (2008) 3692-3696.
[63] R. Palai, R.S. Katiyar, H. Schmid, P. Tissot, S.J. Clark, J. Robertson, S.A.T. Redfern, G. Catalan, J.F. Scott, β phase and γ−β metal-insulator transition in multiferroic BiFeO3, Physical Review B, 77 (2008) 014110.
[64] J.M. Munro, H. Akamatsu, H. Padmanabhan, V.S. Liu, Y. Shi, L.-Q. Chen, B.K. VanLeeuwen, I. Dabo, V. Gopalan, Discovering minimum energy pathways via distortion symmetry groups, Physical Review B, 98 (2018) 085107.
[65] D. Zagorac, J. Zagorac, J.C. Schön, N. Stojanovic, B. Matovic, ZnO/ZnS (hetero)structures: ab initio investigations of polytypic behavior of mixed ZnO and ZnS compounds, Acta Crystallographica B, 74 (2018) 628-642.
[66] S.M. Selbach, T. Tybell, M.-A. Einarsrud, T. Grande, Size-Dependent Properties of Multiferroic BiFeO3 Nanoparticles, Chemistry of Materials, 19 (2007) 6478-6484.
[67] P. Ravindran, R. Vidya, A. Kjekshus, H. Fjellvåg, O. Eriksson, Theoretical investigation of magnetoelectric behavior in BiFeO3, Physical Review B, 74 (2006) 224412.
[68] O. Diéguez, O.E. González-Vázquez, J.C. Wojdeł, J. Íñiguez, First-principles predictions of low-energy phases of multiferroic BiFeO${}_{3}$, Physical Review B, 83 (2011) 094105.
[69] R. Haumont, J. Kreisel, P. Bouvier, F. Hippert, Phonon anomalies and the ferroelectric phase transition in multiferroic BiFeO3, Physical Review B, 73 (2006) 132101.

[70] J. Singh, A. Agarwal, S. Sanghi, P. Prakash, A. Das, C.L. Prajapat, M. Rangi, Phase transformation in crystal and magnetic structure and improved dielectric and magnetic properties of Ho substituted BiFeO3multiferroics, AIP Advances, 9 (2019) 025110.
[71] D.L. Golić, A. Radojković, J. Ćirković, A. Dapčević, D. Pajić, N. Tasić, S.M. Savić, M. Počuča-Nešić, S. Marković, G. Branković, Z.M. Stanojević, Z. Branković, Structural, ferroelectric and magnetic properties of BiFeO3 synthesized by sonochemically assisted hydrothermal and hydro-evaporation chemical methods, Journal of the European Ceramic Society, 36 (2016) 1623-1631.
[72] D.L. Golić, A. Radojković, A. Dapčević, D. Pajić, J. Dragović, F. Torić, J. Ćirković, G. Branković, Z. Branković, Change in structural, ferroelectric, and magnetic properties of bismuth ferrite induced by doping with gadolinium, Ceramics International, 45 (2019) 19158-19165.
[73] A. Radojković, D.L. Golić, J. Ćirković, Z.M. Stanojević, D. Pajić, F. Torić, A. Dapčević, P. Vulić, Z. Branković, G. Branković, Tuning of BiFeO3 multiferroic properties by light doping with Nb, Ceramics International, 44 (2018) 16739-16744.
[74] Y.-H. Lin, Q. Jiang, Y. Wang, C.-W. Nan, L. Chen, J. Yu, Enhancement of ferromagnetic properties in BiFeO3 polycrystalline ceramic by La doping, Applied Physics Letters, 90 (2007) 172507.
[75] G. Catalan, K. Sardar, N.S. Church, J.F. Scott, R.J. Harrison, S.A.T. Redfern, Effect of chemical substitution on the Néel temperature of multiferroic Bi1−xCaxFeO3, Physical Review B, 79 (2009) 212415.
[76] I. Sosnowska, R. Przeniosło, P. Fischer, V.A. Murashov, Investigation of Crystal and Magnetic Structure of BiFeO_{3} Using Neutron Diffraction, Acta Physica Polonica A, 86 (1994) 629-631.
[77] C. Ederer, N.A. Spaldin, Weak ferromagnetism and magnetoelectric coupling in bismuth ferrite, Physical Review B, 71 (2005) 060401.
[78] C. Suchomski, C. Reitz, D. Pajic, Z. Jaglicic, I. Djerdj, T. Brezesinski, Large-Pore Mesoporous Ho3Fe5O12 Thin Films with a Strong Room-Temperature Perpendicular Magnetic Anisotropy by Sol–Gel Processing, Chemistry of Materials, 26 (2014) 2337-2343.
[79] O. Prakash, M.A.H. McCausland, Free precession of 165Ho nuclei in a single crystal of holmium iron garnet, Journal of Physics C: Solid State Physics, 16 (1983) L903.
[80] J. Englich, H. Lütgemeier, M.W. Pieper, K.F.A. Jülich, W. Germany, V. Nekvasil, P. Novák, Umbrella structure in Ho substituted YIG - NMR study, Solid State Communications, 56 (1985) 825-828.